Stefan Frei, Bärbel Holm, Thomas Richter, Thomas Wick, Huidong Yang (Eds.)
Fluid-Structure Interaction

Radon Series on Computational and Applied Mathematics

Volume 20

Fluid-Structure Interaction

Modeling, Adaptive Discretizations and Solvers

Edited by
Stefan Frei,
Bärbel Holm,
Thomas Richter,
Thomas Wick,
Huidong Yang

DE GRUYTER

Editors
Dr. Stefan Frei
Dept. of Mathematics
University College London
Gower Street
London
WC1E 6BT
United Kingdom
s.frei@ucl.ac.uk

Dr. Bärbel Holm
KTH Royal Institute of Technology
Computational Science & Technology
Lindstedtsvägen 5
100 44 Stockholm
Sweden
barbel@kth.se

Prof. Dr. Thomas Richter
Institut für Analysis und Numerik
Universität Magdeburg
Universitätsplatz 2
39106 Magdeburg
Germany
thomas.richter@ovgu.de

A-Prof. Dr. Thomas Wick
Centre de Mathematiques Appliquees (CMAP)
Ecole Polythechnique
Université Paris-Saclay
91128 Palaiseau cedex
France
thomas.wick@cmap.polytechnique.fr

Dr. Huidong Yang
Technische Universität Graz
Institut für Numerische Mathematik
Steyrergasse 30
8010 Graz
Austria
huidong.yang@ricam.oeaw.ac.at

ISBN 978-3-11-049527-0
e-ISBN (PDF) 978-3-11-049425-9
e-ISBN (EPUB) 978-3-11-049258-3
Set-ISBN 978-3-11-049426-6
ISSN 1865-3707

Library of Congress Cataloging-in-Publication Data
A CIP catalog record for this book has been applied for at the Library of Congress.

Bibliographic information published by the Deutsche Nationalbibliothek
The Deutsche Nationalbibliothek lists this publication in the Deutsche Nationalbibliografie; detailed bibliographic data are available on the Internet at http://dnb.dnb.de.

Typesetting: le-tex publishing services GmbH, Leipzig
Printing and binding: CPI books GmbH, Leck
♾ Printed on acid-free paper
Printed in Germany

www.degruyter.com

Preface

In January 2016, we had the pleasure to welcome a number of leading experts and many young researchers working in the field of fluid-structure interactions for a one-week international symposium including a winter school on

Modeling, Adaptive Discretizations and Solvers for Fluid-Structure Interaction

at the Johann Radon Institute for Computational and Applied Mathematics (RICAM) in the beautiful winter in Linz, Austria.

Motivated by the fascinating variety of topics presented in this symposium, we decided to collect nine of them into a book that might serve for future reference. These topics comprise both reviews of state-of-the-art fluid-structure interaction (FSI) as well as very recent research directions and are written by well-known experts in the field.

The aim of this book is a collection of various topics in order to highlight current directions in multiphysics problems. Despite the fact that a lot of progress has been made in the understanding and simulation of FSI in the last decades, FSI is still one of the most challenging topics in numerical mathematics and engineering. A number of open questions and challenges persist, e.g., in the design of efficient and robust solvers for FSI with large deformation and contact as well as regarding the numerical analysis of algorithms and discretization.

In order to facilitate the reading of this book, we classify the articles into three groups:
- Modeling and discretization;
- Solvers;
- Applications.

Despite the challenges of classical FSI on its own, there are several chapters that even go beyond FSI and a couple with further physical phenomena, e.g., thermal and fracture. Nonstandard discretization techniques such as extended ALE, high-resolution interface meshes, Eulerian FSI, and phase-field are addressed. With regard to the numerical solution, insight into monolithic and partitioned approaches is provided. Several applications in vascular flows, binary-fluid-solid interaction, and cracked solids complement the contents.

Finally, we want to thank our sponsors that supported the FSI symposium and finally enabled us to start this book: the Austrian Academy of Sciences (OEAW), Johann Radon Institute for Computational and Applied Mathematics (RICAM) Linz, the Doctoral Program DK W1214 ‘Computational Mathematics’ at the Johannes Kepler University Linz and the graduate school HGS MathComp at the Interdisciplinary Center for Scientific Computing (IWR) in Heidelberg, Germany. We specifically acknowledge

https://doi.org/10.1515/9783110494259-201

Ulrich Langer for scientific and Annette Weihs for administrative support. We also want to mention the unique and friendly atmosphere for the organization of such events at RICAM Linz (which has also been proven by the series of Special Semesters taking place here over the last few years). Last but not least, we thank de Gruyter for their professional and friendly cooperation in producing this book.

Heidelberg, Germany — Stefan Frei
Stockholm, Sweden — Bärbel Holm
Magdeburg, Germany — Thomas Richter
Palaiseau, France; Linz, Austria — Thomas Wick
Graz, Austria; Linz, Austria — Huidong Yang

Contents

Part II: **Solvers**

Part III: **Applications**

List of contributing authors

Johan Hoffman
Department of Computational Science and Technology
School of Computer Science and Communication
KTH Royal Institute of Technology
Stockholm, Sweden
jhoffman@kth.se

Steffen Basting
Institute of Applied Mathematics (LS III)
TU Dortmund
Dortmund, Germany
steffen.basting@math.tu-dortmund.de

Annalisa Quaini
Department of Mathematics
University of Houston
Houston TX, USA
quaini@math.uh.edu

Suncica Canic
Department of Mathematics
University of Houston
Houston TX, USA
E-mail: canic@math.uh.edu

Roland Glowinski
Department of Mathematics
University of Houston
Houston TX, USA.
roland@math.uh.edu

Philipp Birken
Lund University
Center for the Mathematical Sciences
Lund, Sweden
philipp.birken@na.lu.se

Azahar Monge
Lund University
Center for the Mathematical Sciences
Lund, Sweden
azahar.monge@na.lu.se

Ulrich Langer
Johann Radon Institute for Computational and Applied Mathematics
Linz, Austria
ulrich.langer@ricam.oeaw.ac.at

Daniel Jodlbauer
Doctoral Program Computational Mathematics
Johannes Kepler University
Linz, Austria
daniel.jodlbauer@dk-compmath.jku.at

Claudia M. Colciago
MATHICSE, Chair of Modeling and Scientific Computing
École Polytechnique Fédérale de Lausanne
Lausanne, Switzerland
claudia.colciago@epfl.ch

Simone Deparis
MATHICSE, Chair of Modeling and Scientific Computing
École Polytechnique Fédérale de Lausanne
Lausanne, Switzerland
E-mail: simone.deparis@epfl.ch

Davide Forti
MATHICSE, Chair of Modeling and Scientific Computing
École Polytechnique Fédérale de Lausanne
Lausanne, Switzerland
davide.forti@epfl.ch

E. Harald van Brummelen
Eindhoven University of Technology
Eindhoven, The Netherlands
e.h.v.brummelen@tue.nl

Mahnaz Shokrpour Roudbari
Eindhoven University of Technology
Eindhoven, The Netherlands
E-mail: m.shokrpour.roudbari@tue.nl

https://doi.org/10.1515/9783110494259-202

Görkem Şimşek
Eindhoven University of Technology
Eindhoven, The Netherlands
g.simsek@tue.nl

Kristoffer G. van der Zee
School of Mathematical Sciences
The University of Nottingham,
Nottingham, United Kingdom
kg.vanderzee@nottingham.ac.uk3

Part I: **Modeling and discretization**

Steffen Basting, Annalisa Quaini, Suncica Canic, and Roland Glowinski

1 On the implementation and benchmarking of an extended ALE method for FSI problems

Abstract: The simulation of fluid-structure interaction (FSI) problems is particularly challenging when the structural displacement is large. In this situation, certain techniques known to be robust for small structural displacement, such as arbitrary Lagrangian–Eulerian (ALE) methods, fail. Recently, we proposed an *extended ALE* method that overcomes this failure, while keeping the same mesh connectivity and enforcing mesh alignment with the structure. Our extended ALE method relies on a variational mesh optimization technique, where mesh alignment with the structure is achieved via a constraint. Once a mesh has been obtained from the constrained optimization problem, the FSI problem is solved using either a Dirichlet–Neumann algorithm, or a Robin–Neumann algorithm. Here, we provide implementation details for our extended ALE approach, with particular focus on the use of quadratic isoparametric finite elements for a more accurate representation of the fluid-structure interface, an adaptive relaxation procedure based on Aitken's acceleration to speed up the convergence of the Dirichlet–Neumann algorithm, and the structure solver. We validate the structure solver against a benchmark with an exact solution and we assess our extended ALE method through an extensive series of numerical examples involving 2D FSI problems

Keywords: Mesh optimization, Arbitrary Lagrangian–Eulerian formulation, Fluid-structure interaction, Domain decomposition methods

Classification: 74F10, 65N30, 76D05

Note: This research has been supported in part by the NSF under grants DMS-1620384 (Quaini), NIGMS DMS-1263572 (Canic and Quaini), DMS-1613757, DMS-1318763, DMS-1311709 (Canic). The research of Canic was also supported by the UH Cullen Distinguished Professor endowment.

Steffen Basting, Institute of Applied Mathematics (LS III), TU Dortmund, Vogelpothsweg 8, 44227 Dortmund, Germany, steffen.basting@math.tu-dortmund.de
Annalisa Quaini, Department of Mathematics, University of Houston, 4800 Calhoun Rd, Houston TX 77204, USA, quaini@math.uh.edu
Suncica Canic, Department of Mathematics, University of Houston, 4800 Calhoun Rd, Houston TX 77204, USA, canic@math.uh.edu
Roland Glowinski, Department of Mathematics, University of Houston, 4800 Calhoun Rd, Houston TX 77204, USA, roland@math.uh.edu

https://doi.org/10.1515/9783110494259-001

1.1 Introduction

The focus of this work is on the numerical simulation of the motion of an elastic body immersed in an incompressible, viscous fluid, with the structure undergoing large displacements. The motivation comes from fluid-structure interaction (FSI) between blood flow and heart valves. Several difficulties are associated with accurate numerical simulation of this class of fluid-structure interaction problems. Firstly, the coupled multiphysics problem is highly nonlinear and the so-called added mass effect is known to cause various numerical difficulties when the fluid and structure have comparable densities [21, 68]. Then, large changes in the fluid domain occur due to the large structural displacements. Finally, accurate approximation of the hydrodynamic force at the fluid-structure interface is needed to correctly reproduce the physics of the problem. Before outlining how we tackle the above-mentioned difficulties, let us attempt to briefly summarize the vast literature on numerical approaches for this class of problems.

To deal with the fluid domain motion associated with structural displacements, numerical methods can be classified into the methods with fixed meshes and the methods with moving meshes. The fixed mesh methods include the Immersed Boundary Method (IBM) [58–60], the Fictitious Domain Method [1, 39, 40], the level set method [23, 24, 37], and the so-called Eulerian FSI methods [28, 64, 73]. These methods rely on a fixed fluid mesh used in a fluid solver, while the presence of the structure is implemented in different ways. For example, in the IBM the fluid feels the structure through external forces acting on the fluid, where the coupling between the (fixed) fluid mesh and a (Lagrangian) structure mesh is performed via Dirac Delta functions. To get around the difficulties associated with the discretization of the Dirac Delta, and the low accuracy it causes in the calculation of the hydrodynamic force, modifications of the IBM were introduced. They include the extended IBM [71], and the Immersed Finite Element Method [74]. Conversely, in the Fictitious Domain Method, the coupling between the fluid and structure is enforced via Lagrange multipliers (imposing continuity of velocity, or the no-slip condition). This approach was applied first to problems with rigid particles and later to problems with flexible structures, where Lagrange multipliers were located along the structure surface [3, 44, 69, 70]. In all the cases discussed above, adaptive mesh refinement typically needs to be used to obtain reasonable accuracy in the calculation of the hydrodynamic force acting on the structure.

The moving mesh methods are typically based on arbitrary Lagrangian–Eulerian (ALE) approaches, introduced in [25, 47] for FSI problems discretized with the Finite Element method. Earlier works [45, 57] introduced ALE methods for the Navier–Stokes equations in moving domains discretized with the Finite Difference method. Instead of being fixed, the fluid mesh follows the motion of the elastic body via a mapping, called the ALE mapping, which is calculated based on the current location of the structure (e.g., as a harmonic extension of the current interface position onto the fluid domain).

ALE methods were proven to be accurate and robust for hemodynamics applications involving small mesh displacements (e.g., [32]). Although these methods offer many advantages provided by the explicit representation of the fluid-structure interface [7, 46, 68], problems arise whenever strong deformations or even topological changes of the interface lead to a degeneration of the computational mesh. To deal with large structural displacements, "remeshing" was introduced in [27, 52, 53]. By remeshing it is normally meant that a new mesh with different connectivity is generated from scratch when the quality of the given mesh is poor.

Mixed ALE and fictitious domain formulations have also been proposed [26, 43]. These approaches also require adaptive mesh refinement for an accurate calculation of the viscous shear stresses on the solid boundary.

For completeness, we also mention a mesh-free Lattice–Boltzmann method [20, 29, 31, 48], which has also been used for the simulation of FSI problems with large structural displacements.

In the present work we provide implementation details and additional benchmark testing for an extended ALE approach we recently proposed in [10]. Our method captures large structural displacements *without changing mesh connectivity* and it accurately approximates the fluid-structure interface and the hydrodynamic forces *without the need for adaptive mesh refinement*. The method is based on a fixed "base" mesh that is adapted to approximate the interface via an ALE-type mapping, while maintaining mesh connectivity (nodes or elements are neither inserted nor removed). The fundamental building block is a variational mesh optimization approach that does not rely on any combinatorial considerations. Alignment of the optimized mesh with the structure interface is stated as a constraint of a mesh optimization problem thanks to a level set description of the geometry.

The main features of our extended ALE approach are:

- Nondegenerate meshes of provably optimal quality;
- The alignment of the mesh with the interface, which allows for a simple definition and efficient implementation of problem-specific finite element spaces, such as spaces allowing for discontinuities across the interface;
- Fixed mesh connectivity, which makes the method easy to implement in an existing standard ALE code.

We remark that similar approaches to ours are presented in [5, 14, 22] (the fixed-mesh ALE approach) and in [35, 36] (methodology based on "universal meshes" [63]). The main benefits of our variational approach over those in [5, 14, 22, 35, 36] are: *no explicit combinatorial testing* is needed and the resulting *meshes are guaranteed to be nondegenerate*. Once a mesh has been obtained from the above-mentioned constrained optimization problem, the FSI problem is solved with classical Domain Decomposition algorithms (e.g., [62]): either the Dirichlet–Neumann (DN) method, which is combined with an Aitken's acceleration technique [49], or the Robin–Neumann method (RN). Because of the modularity of DN and RN algorithms, each physics subprob-

lem is solved separately, with the coupling conditions enforced in an iterative fashion. We remark that the use of Robin interface conditions has led to efficient partitioned FSI algorithms when the structure lies on part of the fluid domain boundary; see, e.g., [4, 6, 18, 19, 42, 56].

We test our approach through a series of benchmark cases that involve the interaction of an inextensible, elastic beam with a 2D incompressible fluid. We show that our extended ALE method allows one to easily capture the pressure discontinuity across the interface, which coincides with the 1D elastic structure. Methods based on nonaligned fixed meshes cannot capture such a discontinuity, unless further techniques are used, such as, e.g., the enrichment of the function spaces as in X-FEM, see [34]. Moreover, thanks to the mesh alignment with the interface, the coupling conditions required by the Domain Decomposition methods are easily enforced. To treat the structure, we combine a generalized Crank–Nicolson scheme with an Uzawa-type algorithm for solving the saddle-point problem associated with an augmented Lagrangian method employed to handle the inextensibility condition. This nontrivial structure solver is described in Section 1.5.2 and validated against a benchmark with exact solution in Section 1.6.1.

The outline of the paper is as follows. In Section 1.2 we state the problem. The constrained optimization approach, which is at the core of our Extended ALE method, is explained in Section 1.3. We describe the Domain Decomposition algorithms in Section 1.4, and summarize the numerical methods that we use for the time and space discretization of the fluid and structure problems in Section 1.5. In Section 1.6, we present numerical results obtained on a series of numerical tests carefully chosen to highlight the main features of the method. Conclusions are drawn in Section 1.7.

1.2 Problem definition

Consider a time-independent domain $\Omega \subset \mathbb{R}^2$ containing an elastic beam forming a 1D manifold $\Gamma(t) \subset \Omega$ whose location depends on time. The beam is surrounded by an incompressible, viscous fluid occupying domain $\Omega_f(t) := \Omega \setminus \Gamma(t)$. See Figure 1.1.

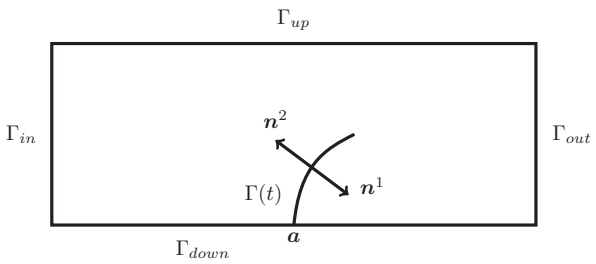

Fig. 1.1: Computational domain.

1.2.1 The fluid problem

The fluid flow is governed by the Navier–Stokes equations for an incompressible, viscous fluid:

$$\rho_{\mathrm{f}}\left(\frac{\partial \boldsymbol{u}}{\partial t} + (\boldsymbol{u}\cdot\nabla)\boldsymbol{u}\right) - \nabla\cdot\boldsymbol{\sigma} = \mathbf{0} \quad \text{in } \Omega_{\mathrm{f}}(t)\,, \tag{1.1}$$

$$\nabla\cdot\boldsymbol{u} = 0 \quad \text{in } \Omega_{\mathrm{f}}(t)\,, \tag{1.2}$$

for $t \in (0, T]$, where ρ_{f} is the fluid density, $\boldsymbol{u}$ is the fluid velocity, and $\boldsymbol{\sigma}$ the Cauchy stress tensor. For Newtonian fluids $\boldsymbol{\sigma}$ has the following expression

$$\boldsymbol{\sigma}(\boldsymbol{u}, p) = -p\mathbf{I} + 2\mu\boldsymbol{\epsilon}(\boldsymbol{u})\,,$$

where p is the pressure, μ is the fluid dynamic viscosity, and $\boldsymbol{\epsilon}(\boldsymbol{u}) = (\nabla\boldsymbol{u} + (\nabla\boldsymbol{u})^T)/2$ is the strain rate tensor. Equations (1.1)–(1.2) need to be supplemented with initial and boundary conditions.

In order to describe the evolution of the fluid domain, we begin by adopting an *Arbitrary Lagrangian–Eulerian* (ALE) approach [47]. More precisely, let $\hat{\Omega}_{\mathrm{f}} \subset \mathbb{R}^2$ be a fixed reference domain. We consider a smooth ALE mapping

$$\mathcal{A} : [0, T] \times \hat{\Omega}_{\mathrm{f}} \to \mathbb{R}^2\,,$$
$$\mathcal{A}(t, \hat{\Omega}_{\mathrm{f}}) = \Omega_{\mathrm{f}}(t)\,, \quad \forall t \in [0, T]\,.$$

For each time instant $t \in [0, T]$, $\mathcal{A}$ is assumed to be a homeomorphism. The domain velocity $\mathbf{w}$ is defined as

$$\mathbf{w}(t, \cdot) = \partial_t \mathcal{A}(t, \mathcal{A}(t, \cdot)^{-1}).$$

For any sufficiently smooth function $F : [0, T] \times \mathbb{R}^2 \to \mathbb{R}$, we may define the ALE time derivative of F as

$$\frac{\partial F}{\partial t}\Big|_{\hat{\mathbf{x}}} = \frac{\partial F}{\partial t}(t, \mathcal{A}(t, \hat{\mathbf{x}})) = \frac{\partial F}{\partial t}(t, \mathbf{x}) + \mathbf{w}(t, \mathbf{x})\cdot\nabla F(t, \mathbf{x}),$$

where $\mathbf{x} = \mathcal{A}(t, \hat{\mathbf{x}})$, $\hat{\mathbf{x}} \in \hat{\Omega}$. With these definitions, we can write the incompressible Navier–Stokes equations in ALE formulation as follows:

$$\rho_{\mathrm{f}}\frac{\partial \boldsymbol{u}}{\partial t}\Big|_{\hat{\mathbf{x}}} + \rho_{\mathrm{f}}(\boldsymbol{u} - \mathbf{w})\cdot\nabla\boldsymbol{u} - \nabla\cdot\boldsymbol{\sigma} = \mathbf{0} \quad \text{in } \Omega_{\mathrm{f}}(t)\,, \tag{1.3}$$

$$\nabla\cdot\boldsymbol{u} = 0 \quad \text{in } \Omega_{\mathrm{f}}(t)\,, \tag{1.4}$$

for $t \in (0, T]$.

1.2.2 The structure problem

For the structure problem, we consider a linearly elastic inextensible beam equation. This means that the beam is not allowed to shrink or stretch while interacting with the

fluid. The motion of an inextensible beam, while well studied (e.g., [26, 38, 41] and references therein), remains a challenging problem numerically. The main difficulty stems from the nonlinearity due to the inextensibility condition.

We assume negligible torsional effects for the beam. Let us denote by ρ_s the linear density (i.e., mass per unit length), by L the length, and by EI the flexural stiffness of the beam. We will use the following notation, with s denoting arc length and t time:

$$\boldsymbol{y}' = \frac{\partial \boldsymbol{y}}{\partial s}\,, \quad \dot{\boldsymbol{y}} = \frac{\partial \boldsymbol{y}}{\partial t}\,, \quad \boldsymbol{y}'' = \frac{\partial^2 \boldsymbol{y}}{\partial s^2}\,, \quad \ddot{\boldsymbol{y}} = \frac{\partial^2 \boldsymbol{y}}{\partial t^2}.$$

Using the virtual work principle, the beam motion for $t \in (0, T]$ is modeled by the following. Find $\boldsymbol{x}(t) \in K$ such that:

$$\int_0^L \rho_s \ddot{\boldsymbol{x}} \cdot \boldsymbol{y} ds + \int_0^L EI\, \boldsymbol{x}'' \cdot \boldsymbol{y}'' ds = \int_0^L \boldsymbol{f} \cdot \boldsymbol{y} ds\,, \quad \forall \boldsymbol{y} \in dK(\boldsymbol{x})\,, \tag{1.5}$$

where $\boldsymbol{x} = \boldsymbol{x}(t, s)$ is the parametric curve defining the beam position, $\boldsymbol{f}$ denotes the force acting on the beam, and

$$K = \left\{ \boldsymbol{y} \in (H^2(0, L))^2, \left|\boldsymbol{y}'\right| = 1,\ \boldsymbol{y}(0) = \boldsymbol{a},\ \boldsymbol{y}'(0) = \boldsymbol{b} \right\}\,, \tag{1.6}$$

$$dK(\boldsymbol{x}) = \left\{ \boldsymbol{y} \in (H^2(0, L))^2,\ \boldsymbol{x}' \cdot \boldsymbol{y}' = 0,\ \boldsymbol{y}(0) = \boldsymbol{0},\ \boldsymbol{y}'(0) = \boldsymbol{0} \right\}\,. \tag{1.7}$$

In our case, $\boldsymbol{f}$ is the hydrodynamic force, which will be specified in Section 1.2.3. For problem (1.5) we choose boundary conditions

$$\boldsymbol{x}(0) = \boldsymbol{a}\,, \quad \boldsymbol{x}'(0) = \boldsymbol{b}\,, \quad \boldsymbol{x}''(L) = \boldsymbol{x}'''(L) = 0\,. \tag{1.8}$$

The conditions at $s = 0$ are called the *essential boundary conditions*, describing a clamped beam, while the conditions at $s = L$ are called the *natural boundary conditions*. The nonlinear inextensibility condition for the beam, $|\boldsymbol{x}'| = 1$, is embedded into the set K.

1.2.3 The coupled fluid-structure interaction problem

We consider two-way coupling between the fluid and structure: the motion of the beam is driven by the contact force exerted by the fluid, while at the same time the motion of the beam influences the fluid motion. The coupling conditions are described by the following. Let us denote the interface by

$$\Gamma(t) = \{\boldsymbol{x}(t, s),\ s \in [0, L]\}\,.$$

Let $\boldsymbol{n}^1$ be the unit normal vector pointing to the "left" (left with respect to the parameterization of $\boldsymbol{x}$) and $\boldsymbol{n}^2 = -\boldsymbol{n}^1$ be the unit normal pointing to the "right", see Figure 1.1.

Notice that the fluid-structure interface coincides with the structure domain. The hydrodynamic force acting on the structure (beam) is given by the jump in the normal fluid stress across the interface $\Gamma(t)$:

$$\boldsymbol{f}_\Gamma = -\boldsymbol{\sigma}^1\boldsymbol{n}^1 - \boldsymbol{\sigma}^2\boldsymbol{n}^2 \,, \tag{1.9}$$

where $\boldsymbol{\sigma}^i(\mathbf{x}) = \lim_{\epsilon\to 0^-} \boldsymbol{\sigma}(\mathbf{x}+\epsilon\boldsymbol{n}^i)$, $\mathbf{x} \in \Gamma$, $i = 1, 2$. Using this notation, we can now state the coupling conditions. For $t \in (0, T]$, the fluid problem (1.3),(1.4) and the structure problem (1.5) are coupled by the following two conditions:

1. kinematic coupling condition (continuity of velocity, i.e., the no-slip condition)

$$\boldsymbol{u} = \dot{\boldsymbol{x}} \quad \text{on } \Gamma(t) \,; \tag{1.10}$$

2. dynamic coupling condition (balance of contact forces)

$$\boldsymbol{f}_\Gamma = \boldsymbol{f} \quad \text{on } \Gamma(t) \,, \tag{1.11}$$

   where $\boldsymbol{f}$ is given by Equation (1.5).

Here, notation $\boldsymbol{u} = \dot{\boldsymbol{x}}$ in (1.10) is used to express the relation $\boldsymbol{u}(t, \boldsymbol{x}(t, s)) = \dot{\boldsymbol{x}}(t, s)$, $s \in [0, L]$ (analogously for $\boldsymbol{f}_\Gamma$ and $\boldsymbol{f}$ in (1.11)). Since $\boldsymbol{x}$ denotes the location of structure points and not the structure displacement, both the structure and fluid are given in Eulerian coordinates.

For the purposes that will be clear below when we introduce the Robin–Neumann scheme, we remark here that the coupling conditions (1.10)–(1.11) can be written in an equivalent form by introducing the constants $\alpha_\mathrm{f} > 0$ and $\alpha_\mathrm{s} > 0$ ($\alpha_\mathrm{f} \neq \alpha_\mathrm{s}$), and writing:

$$\begin{aligned} \alpha_\mathrm{f}\boldsymbol{u} - \boldsymbol{f}_\Gamma &= \alpha_\mathrm{f}\dot{\boldsymbol{x}} - \boldsymbol{f} \quad \text{on } \Gamma(t) \,, \\ \alpha_\mathrm{s}\boldsymbol{u} + \boldsymbol{f} &= \alpha_\mathrm{s}\dot{\boldsymbol{x}} + \boldsymbol{f}_\Gamma \quad \text{on } \Gamma(t). \end{aligned} \tag{1.12}$$

1.3 Numerical representation of the geometry

The main feature of our extended ALE method is a variational mesh optimization technique combined with an additional constraint to enforce the alignment of the structure interface with the edges of the resulting triangulation. The mesh optimization in this section corresponds to a reparametrization of the ALE mapping.

1.3.1 Optimal triangulations

Let $\mathcal{T}$ be an initial, reference triangulation of the domain Ω (not necessarily approximating the structure interface at this stage). Following a variational mesh optimization technique introduced by M. Rumpf in [65], we aim at finding an "optimal" triangulation $\mathcal{T}_\mathrm{opt}$ resulting from an optimal mesh deformation χ_opt of $\mathcal{T}$, i.e., $\mathcal{T}_\mathrm{opt} = \chi_\mathrm{opt}(\mathcal{T})$.

Deformation χ_{opt} belongs to the set D of piecewise affine, orientation preserving, and globally continuous deformations:

$$D = \left\{ \chi \in \left(\mathcal{C}^0(\Omega) \right)^2 : \nabla\chi|_T \in \mathrm{GL}(2),\ \det(\nabla\chi|_T) > 0,\ \forall T \in \mathcal{T} \right\} , \tag{1.13}$$

with $\mathrm{GL}(2) = \{A \in \mathbb{R}^{2\times 2} :\ \det(A) \neq 0\}$.

Deformation $\chi_{\text{opt}} \in D$ is "optimal" in the sense that it is the argument for which a certain functional $\mathcal{F}$ attains its minimum value:

$$\mathcal{F}(\chi_{\text{opt}}) = \min_{\chi \in D} \mathcal{F}(\chi) . \tag{1.14}$$

We assume that the functional in (1.14) can be represented by a sum of weighted, element-wise contributions F_T:

$$\mathcal{F}(\chi) = \sum_{T \in \mathcal{T}} \mu_T F_T(\chi) ,$$

where $\mu_T > 0$ denotes a positive weight with $\sum_T \mu_T = 1$. Let R_T denote the linear reference mapping from a prescribed reference element T_{opt} (an equilateral simplex with customizable edge length h) to T. Under the assumptions of translational invariance, isotropy and frame indifference of the functionals, it can be shown that in two dimensions F_T may be expressed as a function of the invariants of χ: $\|\nabla R_T(\chi)\|^2$ and $\det(\nabla R_T(\chi))$ [65]. For example, given a function $\tilde{F}_T : \mathbb{R} \times \mathbb{R} \to \mathbb{R}$ we can write:

$$F_T(\chi) = \tilde{F}_T(a, d) := \tilde{F}_T(\|\nabla R_T(\chi)\|^2, \det(\nabla R_T(\chi))) .$$

Here, $\|\cdot\|$ denotes the Frobenius norm. Note that the quantity $\|\nabla R_T(\chi)\|^2$ measures the change of edge lengths with respect to the reference element, and $\det(\nabla R_T(\chi))$ measures the change in area.

In order to rule out deformations with vanishing determinant, we need

$$\lim_{\det(\nabla R_T(\chi)) \to 0} F_T(\chi) = \infty .$$

With the additional assumption that the local functional $F_T(\chi) = \tilde{F}_T(a, d)$ is polyconvex (i.e., $\tilde{F}_T(a, d)$ is convex with respect to each argument), it can be proven that an optimal deformation exists and is globally injective [65].

A classical example of such a function F_T is given by

$$F_T(\chi) = (\|\nabla R_T(\chi)\|^2 - 2)^2 + \det(\nabla R_T(\chi)) + \frac{1}{\det(\nabla R_T(\chi))} . \tag{1.15}$$

The optimally deformed simplex is obtained if $\chi_{\text{opt}}|_T = \mathbf{I}$, i.e., if

$$F_T(\chi_{\text{opt}}) = F_T(\mathbf{I}) = (2 - 2)^2 + 1 + 1 = 2 .$$

The variational mesh smoothing approach described above has several advantages:

- Minimization problem (1.14) yields triangulations that are provably optimal in the sense of the local measure (1.15).
- These triangulations can be shown to be nondegenerate, i.e., no self-intersection of elements occurs. This is the main property needed by our mesh optimization approach in order to work reliably even when the structure displacement is large.
- The element-wise representation of $\mathcal{F}$ provides built-in, local mesh quality control.

The price to pay for those advantages is that functional $\mathcal{F}$ in (1.14) is highly nonlinear, nonconvex, and global minimizers may not be unique.

1.3.2 Interface aligned mesh

We are now interested in having a triangulation that is nondegenerate, optimal (as explained in the previous subsection) *and* aligned with the beam position $\Gamma(t)$, i.e., we want the optimal triangulation edges to approximate $\Gamma(t)$. For this purpose, we introduce the following auxiliary tools:

- a "tubular box" around the structure of width δ, denoted by $\Omega_{\mathrm{f}}^{\delta}(t) \subset \Omega_{\mathrm{f}}(t)$, within which mesh optimization with alignment will be performed, see Figure 1.2a;
- a continuous level set function $\phi\colon [0,T]\times\Omega_{\mathrm{f}}^{\delta}(t) \to \mathbb{R}$ whose zero level set includes the structure position $\boldsymbol{x}$:

$$\begin{aligned} \Omega_{\mathrm{f}}^{\delta,1}(t) &= \left\{\boldsymbol{y} \in \Omega_{\mathrm{f}}^{\delta}(t)\colon \phi(t,\boldsymbol{y}) > 0\right\}, \\ \Omega_{\mathrm{f}}^{\delta,2}(t) &= \left\{\boldsymbol{y} \in \Omega_{\mathrm{f}}^{\delta}(t)\colon \phi(t,\boldsymbol{y}) < 0\right\}, \\ \Gamma^{\delta}(t) &= \left\{\boldsymbol{y} \in \Omega_{\mathrm{f}}^{\delta}(t)\colon \phi(t,\boldsymbol{y}) = 0\right\}, \end{aligned} \tag{1.16}$$

where $\Gamma^{\delta}(t)$ denotes a "natural" extension of $\Gamma(t)$ to the boundary of $\Omega_{\mathrm{f}}^{\delta}(t)$, and $\Omega_{\mathrm{f}}^{\delta,1}(t)$ and $\Omega_{\mathrm{f}}^{\delta,2}(t)$ denote the fluid subdomains located on the "left" and "right" side of $\Gamma^{\delta}(t)$, respectively. See Figure 1.2a. Notice that $\boldsymbol{n}^1$ (resp., $\boldsymbol{n}^2$) is the outward unit normal on $\Gamma^{\delta}(t)$ of $\Omega_{\mathrm{f}}^{\delta,1}(t)$ (resp., $\Omega_{\mathrm{f}}^{\delta,2}(t)$).

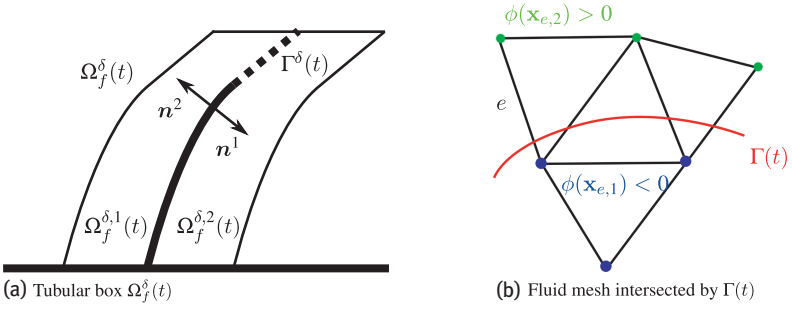

(a) Tubular box $\Omega_f^{\delta}(t)$ (b) Fluid mesh intersected by $\Gamma(t)$

Fig. 1.2: (a) Tubular box $\Omega_{\mathrm{f}}^{\delta}(t)$ around the structure position $\boldsymbol{x}$, zoomed in view of Figure 1.1, and (b) $\Gamma(t)$ intersecting elements of the fluid mesh.

Within $\Omega_f^\delta(t)$ we perform the following procedure. Let e be an arbitrary edge of the triangulation $\mathcal{T}$ intersected by $\Gamma^\delta(t)$ as shown in Figure 1.2b, and let $\mathbf{x}_{e,1}$ and $\mathbf{x}_{e,2}$ be its endpoints. Because of continuity of ϕ and assumption (1.16), we observe that

$$\phi(\mathbf{x}_{e,1})\phi(\mathbf{x}_{e,2}) < 0$$

if and only if e is intersected by $\Gamma^\delta(t)$, provided that the mesh size h is sufficiently small to resolve the shape of $\Gamma^\delta(t)$. We therefore define the triangulation to be *linearly aligned* with $\Gamma(t)$ if

$$\phi(\mathbf{x}_{e,1})\phi(\mathbf{x}_{e,2}) \geq 0 \quad \text{for all} \quad e \in \mathcal{T}\,.$$

We introduce a scalar constraint $c\colon D \to \mathbb{R}_0^+$, defined on D given by (1.13), such that:

$$c(\chi) = \sum_{e\in\chi(\mathcal{T})} \mathcal{H}(\phi(\mathbf{x}_{e,1})\phi(\mathbf{x}_{e,2})) \quad \text{where} \quad \mathcal{H}(z) = \begin{cases} > 0 & \text{if } z < 0\,, \\ = 0 & \text{otherwise.} \end{cases}$$

Only deformations χ for which $c(\chi) = 0$ will give aligned triangulations. Thus, a linearly aligned triangulation of optimal quality is obtained from the following constrained minimization problem:

$$\min_{\chi\in D} \mathcal{F}(\chi) \quad \text{such that} \quad c(\chi) = 0\,.$$

Given an aligned triangulation $\mathcal{T}$, we may define a linear approximation of the interface as

$$\Gamma_h = \{\text{edges } e \in \mathcal{T}\colon \phi(\mathbf{x}_{e,i}) = 0 \quad \text{and} \quad \mathbf{x}_{e,i} \in \Gamma \text{ for } i = 1, 2\}\,.$$

Note that condition $\mathbf{x}_{e,i} \in \Gamma$ is necessary to avoid considering points on the extension Γ^δ that do not belong to Γ.

In order to obtain a more accurate representation of the structure, we also consider piecewise quadratic approximations of $\Gamma(t)$ and make use of quadratic isoparametric finite elements. We denote by $\hat{K} = \left\{\hat{\mathbf{x}} \in \mathbb{R}^2\colon \sum_{i=1}^2 \hat{x}^{(i)} \leq 1, \hat{x}^{(i)} \geq 0\right\}$ the reference simplex, and by $G_K\colon \hat{K} \to K$ the quadratic isoparametric mapping:

$$G_K(\hat{\mathbf{x}}) = \sum_{i=1}^{6} \mathbf{x}_i \varphi_i(\hat{\mathbf{x}})\,, \tag{1.17}$$

where φ_i, $i = 1, \ldots, 6$ are the quadratic Lagrange basis functions defined on $\hat{K}$. Once a linearly aligned triangulation and the corresponding discrete interface are obtained, in order to achieve quadratic alignment we move each quadratic node (e.g., $\mathbf{x}_6$ in Figure 1.3) along the linear normal to the zero level set. Details on the numerical implementation together with an evaluation of the mesh, approximation quality, and computational costs can be found in [8, 11, 72].

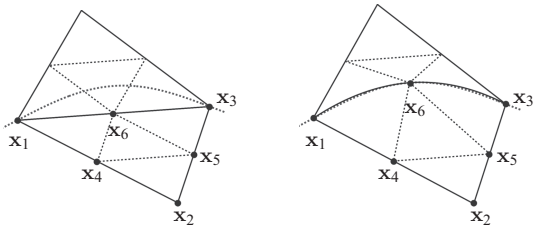

Fig. 1.3: Linearly aligned triangulation with isoparametric elements without (left) and with (right) quadratic alignment of the additional quadratic degree of freedom $\mathbf{x}_6$.

In the following, for a given structure position $\Gamma(t)$, we will denote the optimal interface aligned triangulation obtained from the strategy outlined above by $\mathcal{T}_{\text{opt}}(\Gamma(t))$. The resulting computational domain is given by:

$$\Omega_{\text{f,opt}}(t) = \bigcup_{K \in \mathcal{T}_{\text{opt}}(\Gamma(t))} K \, .$$

1.4 Partitioned methods for the fluid-structure interaction problem

The FSI problems described in Section 1.2 will be solved using two different partitioned strategies based on Domain Decomposition methods [62]: the Dirichlet–Neumann (DN) and the Robin–Neumann (RN) algorithms. Partitioned methods are appealing for solving multiphysics problems such as those discussed in this manuscript, because they allow the reuse of existing fluid and structure solvers with minimal modifications. Because of the modularity of DN and RN algorithms, each physics subproblem is solved separately, with the coupling conditions enforced in an iterative fashion. In the DN algorithm the coupling boundary condition (1.10) is imposed at the interface as a Dirichlet boundary condition for the fluid subproblem, whereas in the RN algorithm the fluid subproblem is endowed with a Robin interface condition (1.12). In both algorithms, the structure subproblem is supplemented with the Neumann "boundary condition" (1.11). Equation (1.11) is a proper Neumann boundary condition when the structure is thick; for thin structures Equation (1.11) prescribes the load on the structure.

To describe the DN and RN algorithms, we introduce the time-discretization step $\Delta t > 0$ and set $t^n = n\Delta t$, for $n = 1, \ldots, N$, with $N = T/\Delta t$. At every time t^n, the DN and RN algorithms iterate over the fluid and structure subproblems until convergence. These are Richardson (also called fixed point) iterations for the position of $\Gamma(t^n)$. Let k be the index for these subiterations.

1.4.1 The Dirichlet–Neumann method

At time t^{n+1}, subiteration $k+1$, assuming that Ω_{f}^n, $\boldsymbol{u}_k$, p_k, and $\boldsymbol{x}_k$ are known, the following steps are performed:

- **Step 1**: Solve the fluid subproblem for the flow variables $\boldsymbol{u}_{k+1}$, p_{k+1} defined on Ω_{f}^n, with **Dirichlet boundary condition**

$$\boldsymbol{u}_{k+1} = \dot{\boldsymbol{x}}_k \quad \text{on} \quad \Gamma^n \,. \tag{1.18}$$

- **Step 2**: Solve the structure subproblem for the structure position $\boldsymbol{x}_{k+1}$, driven by the just calculated hydrodynamic force $\boldsymbol{f}_{\Gamma,k+1}$, i.e., $\boldsymbol{f}_{k+1} = \boldsymbol{f}_{\Gamma,k+1}$ on Γ^n.
- **Step 3**: Check the stopping criterion, e.g.,

$$\frac{\|\boldsymbol{x}_{k+1} - \boldsymbol{x}_k\|}{\|\boldsymbol{x}_k\|} < \epsilon_{\mathrm{FS}} \,, \tag{1.19}$$

  where ϵ_{FS} is a given stopping tolerance. If violated, repeat Steps 1–3. If satisfied, set $\boldsymbol{x}^{n+1} = \boldsymbol{x}_{k+1}$ and $p^{n+1} = p_{k+1}$.
- **Step 4**: Check the mesh quality of Ω_{f}^n. A mesh is considered to be "bad" if the maximum angle of the elements exceeds a certain value, for instance 130 degrees.
  - If the mesh is good: Accept and set $\tilde{\boldsymbol{u}}^{n+1} = \boldsymbol{u}_{k+1}$ and $\tilde{\Omega}_{\mathrm{f}}^{n+1} = \Omega_{\mathrm{f}}^n$.
  - If the mesh is bad: Apply mesh optimization to get $\Omega_{\mathrm{f,opt}}^n$, set $\tilde{\Omega}_{\mathrm{f}}^{n+1} = \Omega_{\mathrm{f,opt}}^n$. Project data onto new mesh, i.e.,

$$\tilde{\boldsymbol{u}}^{n+1} = I_{\Omega_{\mathrm{f}}^n \to \tilde{\Omega}_{\mathrm{f}}^{n+1}}(\boldsymbol{u}_{k+1}) \,. \tag{1.20}$$

- **Step 5:** Standard ALE update: From the new structure position $\boldsymbol{x}^{n+1}$ obtain Γ^{n+1}, and from the intermediate fluid domain $\tilde{\Omega}_{\mathrm{f}}^{n+1}$ obtain:

$$\Omega_{\mathrm{f}}^{n+1} = E\left(\Gamma^{n+1}, \tilde{\Omega}_{\mathrm{f}}^{n+1}\right)$$

  using an extension operator E (see below). Set $\boldsymbol{u}^{n+1} = \tilde{\boldsymbol{u}}^{n+1}$ and move to the next time step.

Notice that if the quality of the mesh is good, that is if the second item at Step 4 never applies, the method reduces to a standard ALE approach. We do not use a "standard" extension operator E (such as harmonic extension, or operators stemming from linear elasticity), but use the variational approach based on (1.14), (1.15). In our experience, this approach is superior to linear extension operators in terms of mesh quality.

In the "inner" loop, which corresponds to Steps 1–3 in the above iteration algorithm, the fluid domain is "frozen", which provides important saving of computational time. Concerning Step 4, the angle-based criterion used to detect "bad" meshes is purely heuristic and may be replaced by other meaningful mesh quality criteria. The criterion should be sufficiently mild in order to prevent the reparametrization at every time step. Notice that the mesh optimization procedure presented in Subsec. 1.3.1 aims

at generating triangulations made of equilateral triangles, therefore the angles after optimization are usually bounded away from, e.g., 130 degrees.

A crucial point in the above algorithm is the choice of the mesh transfer operator $I_{\Omega_f^n \to \tilde{\Omega}_f^{n+1}}$ appearing in Equation (1.20) at Step 4, needed whenever reparametrization is performed. In our case, this operator is the Lagrange interpolation operator which was also proposed in [35]. However, it is known that dynamically changing meshes may lead to spurious oscillations of the pressure for small time-step sizes [15, 17]. Indeed, we will observe those oscillations in our numerical results, as shown in Section 1.6.3. The use of special elements (e.g., divergence-free) or special variational formulations of the Navier–Stokes equations (see for instance [51]) might cure this problem which seems to be an open question.

It is well known that the convergence properties of the DN algorithm depend heavily on the added-mass effect [21]. In fact, when the structure constitutes a part of the fluid domain boundary, the number of DN iterations required to satisfy the stopping criterion (1.19) increases as the structure density approaches the fluid density. Moreover, below a certain density ratio ρ_s/ρ_f, which depends on the domain geometry, relaxation is needed for the DN algorithm to converge [21, 54, 55]. This is why we adopt a simple Aitken's acceleration technique, which is based on a relaxation approach, and is known to reduce the number of DN iterations. This strategy, introduced in [49], was proposed for a setting similar to ours in [2].

Let $\tilde{\boldsymbol{x}}_{k+1}$ be the unrelaxed structure position predicted by Step 2 of the algorithm above. Then after Step 2, we introduce a relaxation parameter ω_{k+1}, which is computed via

$$\omega_{k+1} = \frac{(\boldsymbol{x}_k - \boldsymbol{x}_{k-1}) \cdot (\boldsymbol{x}_k - \tilde{\boldsymbol{x}}_{k+1} - \boldsymbol{x}_{k-1} + \tilde{\boldsymbol{x}}_k)}{|\boldsymbol{x}_k - \tilde{\boldsymbol{x}}_{k+1} - \boldsymbol{x}_{k-1} + \tilde{\boldsymbol{x}}_k|^2} .$$

The position of the interface is then corrected via the relaxation algorithm:

$$\boldsymbol{x}_{k+1} = \omega_{k+1}\tilde{\boldsymbol{x}}_{k+1} + (1 - \omega_{k+1})\,\boldsymbol{x}_k .$$

The results in [2] indicate that only a few accelerated DN subiterations are to be expected for FSI problems with an immersed structure and large added-mass effect.

It was shown in [4] that when the structure constitutes a part of the fluid domain boundary for a suitable choice of parameter α_f the RN method features excellent convergence properties: it always converges without any relaxation and its convergence is insensitive to the added-mass effect. In the next section, we present the RN method.

1.4.2 The Robin–Neumann method

At time t^{n+1}, subiteration $k+1$, the following steps are performed:

– **Step 1**: Solve the fluid subproblem for the flow variables $\boldsymbol{u}_{k+1}$, p_{k+1} defined on Ω_{f}^n, with **Robin boundary condition**

$$\alpha_{\mathrm{f}}\boldsymbol{u}_{k+1} - \boldsymbol{f}_{\Gamma,k+1} = \alpha_{\mathrm{f}}\dot{\boldsymbol{x}}_k - \boldsymbol{f}_k \quad \text{on} \quad \Gamma^n \,. \tag{1.21}$$

– **Step 2**, **3**, **4** and **5** as in Section 1.4.1

Recall that $\boldsymbol{f}_\Gamma$ denotes the jump in the normal stress across the structure, as defined in (1.9), and $\boldsymbol{f}$ stands for the right-hand side of the structure equation (1.5). Notice that the DN algorithm can be interpreted as a particular case of the RN algorithm for $\alpha_{\mathrm{f}} \to \infty$.

In [4], α_{f} is estimated by considering a simplified structure model. Here, we follow the same approach and set the constant α_{f} in (1.21):

$$\alpha_{\mathrm{f}} = \frac{\rho_{\mathrm{s}}}{\Delta t} \,. \tag{1.22}$$

1.5 The fully discrete problem

We present the fully discrete problem for the case of the fluid problem (1.3),(1.4) with Robin boundary condition (1.21), and recall that a similar approach can be taken for the DN algorithm, since it is a particular case of the RN algorithm. We will state the problem in weak form by including only the boundary condition on $\Gamma(t)$, since those on $\partial\Omega$ are understood and do not affect the presented methodology.

1.5.1 The discrete fluid subproblem

For any given $t \in [0, T)$, we define the following spaces:

$$V(t) = \left\{\boldsymbol{v}\colon \Omega_{\mathrm{f}}(t) \to \mathbb{R}^2,\ \boldsymbol{v} = \hat{\boldsymbol{v}} \circ (\mathcal{A})^{-1},\ \hat{\boldsymbol{v}} \in (H^1(\hat{\Omega}_{\mathrm{f}}))^2\right\} \,,$$
$$Q(t) = \left\{q\colon \Omega_{\mathrm{f}}(t) \to \mathbb{R},\ q = \hat{q} \circ (\mathcal{A})^{-1},\ \hat{q} \in L^2(\hat{\Omega}_{\mathrm{f}})\right\} \,.$$

In the following, we will use the notation $V^n := V(t^n)$ and $Q^n := Q(t^n)$ to denote the finite element spaces at the time instant t^n.

We introduce the following linear forms:

$$m(\Omega; \boldsymbol{u}, \boldsymbol{v}) = \int_\Omega (\boldsymbol{u}\cdot\boldsymbol{v})\,\mathrm{d}\Omega \,, \quad a(\Omega; \boldsymbol{u}, \boldsymbol{v}) = \int_\Omega \mu\,(\boldsymbol{\epsilon}(\boldsymbol{u})\colon \boldsymbol{\epsilon}(\boldsymbol{v}))\,\mathrm{d}\Omega \,,$$
$$c(\Omega; \mathbf{w}; \boldsymbol{u}, \boldsymbol{v}) = \int_\Omega ((\mathbf{w}\cdot\nabla)\,\boldsymbol{u}\cdot\boldsymbol{v})\,\mathrm{d}\Omega \,, \quad b(\Omega; p, \boldsymbol{v}) = -\int_\Omega p\nabla\cdot\boldsymbol{v}\,\mathrm{d}\Omega \,.$$

The variational formulation of the fluid problem (1.3), (1.4) with boundary condition (1.12) reads: given $t \in (0, T]$, find $(\boldsymbol{u}, p) \in V(t)\times Q(t)$ such that $\forall(\boldsymbol{v}, q) \in V(t)\times Q(t)$

the following holds:

$$\rho_{\mathrm{f}} m\Big(\Omega_{\mathrm{f}}(t); \frac{\partial \boldsymbol{u}}{\partial t}\Big|_{\hat{\mathbf{x}}}, \boldsymbol{v}\Big) + \rho_{\mathrm{f}} c(\Omega_{\mathrm{f}}(t); \boldsymbol{u} - \mathbf{w}; \boldsymbol{u}, \boldsymbol{v}) + a(\Omega_{\mathrm{f}}(t); \boldsymbol{u}, \boldsymbol{v}) + b(\Omega_{\mathrm{f}}(t); p, \boldsymbol{v})$$
$$+ m(\Gamma(t); \alpha_{\mathrm{f}} \boldsymbol{u}, \boldsymbol{v}) = m(\Gamma(t); \alpha_{\mathrm{f}} \dot{\boldsymbol{x}} - \boldsymbol{f}, \boldsymbol{v}),$$
$$b(\Omega_{\mathrm{f}}(t); q, \boldsymbol{u}) = 0.$$

Time and space discretization. For simplicity, the implicit Euler scheme is used to discretize the above weak formulation in time. The convective term is linearized by a first-order extrapolation formula. Notice that higher order discretization schemes and extrapolation formulas are also possible. At time t^{n+1}, and at the $(k+1)$-st RN subiteration, the time discrete linearized fluid subproblem reads as follows: Find $(\boldsymbol{u}_{k+1}, p_{k+1}) \in V^n \times Q^n$ such that

$$\rho_{\mathrm{f}} m\Big(\Omega_{\mathrm{f}}^n; \frac{\boldsymbol{u}_{k+1} - \boldsymbol{u}^n}{\Delta t}, \boldsymbol{v}\Big) + \rho_{\mathrm{f}} c(\Omega_{\mathrm{f}}^n; \boldsymbol{u}_k - \mathbf{w}^n; \boldsymbol{u}_{k+1}, \boldsymbol{v}) + a(\Omega_{\mathrm{f}}^n; \boldsymbol{u}_{k+1}, \boldsymbol{v})$$
$$+ b(\Omega_{\mathrm{f}}^n; p_{k+1}, \boldsymbol{v}) + m(\Gamma^n; \alpha_{\mathrm{f}} \boldsymbol{u}_{k+1}, \boldsymbol{v}) = m(\Gamma^n; \alpha_{\mathrm{f}} \dot{\boldsymbol{x}}_k - \boldsymbol{f}_k, \boldsymbol{v}) \,, \tag{1.23}$$
$$b(\Omega_{\mathrm{f}}^n; q, \boldsymbol{u}_{k+1}) = 0 \,, \tag{1.24}$$

for all $(\boldsymbol{v}, q) \in V^n \times Q^n$.

For the space discretization of problems (1.23)–(1.24), we choose the inf-sup stable Taylor–Hood finite element pair $\mathbb{P}_2 - \mathbb{P}_1$. However, while the velocity field is continuous at Γ^n, the pressure space should be able to capture discontinuities across Γ^n, which are needed also for the correct evaluation of the hydrodynamic force (1.9). In order to deal with pressure discontinuities that occur at Γ^n, we introduce the following spaces which consist of piecewise continuous functions that may be discontinuous across the interface:

$$\tilde{V}_h^n = \Big\{ \boldsymbol{v} \in (H^1(\Omega_{\mathrm{f}}^n \backslash \Gamma^n)^2 : \ \boldsymbol{v}|_K \circ G_K \in \mathbb{P}_2(\hat{K}), \boldsymbol{v}|_{\Omega_{\mathrm{f}}^n \backslash \Gamma^n} \in \Big(C^0(\Omega_{\mathrm{f}}^n \backslash \Gamma^n) \Big)^2 \Big\} \,,$$
$$\tilde{Q}_h^n = \Big\{ q \in L^2(\Omega_{\mathrm{f}}^n \backslash \Gamma^n), \ q|_K \circ G_K \in \mathbb{P}_1(\hat{K}), \ q|_{\Omega_{\mathrm{f}}^n \backslash \Gamma^n} \in C^0(\Omega_{\mathrm{f}}^n \backslash \Gamma^n) \Big\} \,,$$

where $\hat{K}$ is the reference simplex, and G_K is given by (1.17). The respective spaces with globally continuous functions will be denoted by V_h^n and Q_h^n. The appropriate finite element space for the unknowns in problems (1.23)–(1.24) is given by $V_h^n \times \tilde{Q}_h^n$. For the numerical implementation of our approach, we adopt a strategy called the Subspace Projection method [12, 13, 61]: we will work with spaces $\tilde{V}_h^n$ and $\tilde{Q}_h^n$, and then use an additional discrete projection to enforce continuity of the velocity on Γ^n. Note that V_h^n is a vector subspace of space $\tilde{V}_h^n$.

Let us briefly summarize how the Subspace Projection method works. We first notice that the Oseen problem (1.23) can be formally expressed as: Find $(\boldsymbol{u}_{k+1}, p_{k+1}) \in V^n \times Q^n$ such that

$$s((\boldsymbol{u}_{k+1}, p_{k+1}), (\boldsymbol{v}, q)) = g(\boldsymbol{v}, q) \,, \quad \forall (\boldsymbol{v}, q) \in V^n \times Q^n \,, \tag{1.25}$$

where $s\colon (V^n \times Q^n) \times (V^n \times Q^n) \to \mathbb{R}$ is the bilinear form containing all the terms with index $k+1$, and $g\colon (V^n \times Q^n) \to \mathbb{R}$ is a linear form containing all the terms involving known quantities. Next, we define a projection operator:

$$\mathcal{P}: \tilde{V}_h^n \to V_h^n,$$

where V_h^n is a vector subspace of space $\tilde{V}_h^n$. By the Subspace Projection method, a discrete counterpart of problem (1.25) reads: Find $(\tilde{\boldsymbol{u}}_{h,k+1}, \tilde{p}_{h,k+1}) \in \tilde{V}_h^n \times \tilde{Q}_h^n$ such that

$$s((\mathcal{P}\tilde{\boldsymbol{u}}_{h,k+1}, \tilde{p}_{h,k+1}), (\mathcal{P}\tilde{\boldsymbol{v}}_h, \tilde{q}_h)) = g(\mathcal{P}\tilde{\boldsymbol{v}}_h, \tilde{q}_h)\,, \quad \forall (\tilde{\boldsymbol{v}}_h, \tilde{q}_h) \in \tilde{V}_h^n \times \tilde{Q}_h^n,$$

and then set $\boldsymbol{u}_{h,k+1} = \mathcal{P}\tilde{\boldsymbol{u}}_{h,k+1}$ and $p_{h,k+1} = \tilde{p}_{h,k+1}$. See [12, 13, 61] for a detailed description of these techniques.

The linear system resulting from linearization and discretization is solved with the direct solver PARDISO [50, 66, 67].

1.5.2 The discrete structure problem

For the time discretization of problem (1.5), we will consider a generalized Crank–Nicolson scheme [41]. At time t^{n+1}, Dirichlet–Neumann iteration $k+1$, the time discrete structure problem (1.5) is as follows: Find $\boldsymbol{x}_{k+1} \in K$ such that:

$$\begin{aligned}
&\int_0^L \rho_s \frac{\boldsymbol{x}_{k+1} - 2\boldsymbol{x}^n + \boldsymbol{x}^{n-1}}{\Delta t^2} \cdot \boldsymbol{y} ds + EI \int_0^L (\alpha \boldsymbol{x}_{k+1} + (1-2\alpha)\boldsymbol{x}^n + \alpha \boldsymbol{x}^{n-1})'' \cdot \boldsymbol{y}'' ds \\
&= \int_0^L (\alpha \boldsymbol{f}_{k+1} + (1-2\alpha)\boldsymbol{f}^n + \alpha \boldsymbol{f}^{n-1}) \cdot \boldsymbol{y} ds\,, \quad \forall \boldsymbol{y} \in dK(\boldsymbol{x}_{k+1}),
\end{aligned} \tag{1.26}$$

where K and dK are defined in (1.6) and (1.7), respectively. This scheme is known to be second-order accurate for linear problems. For the numerical results in Section 1.6, we will set $\alpha = 1/4$ since in linear cases this choice leads to an unconditionally stable scheme, which possesses a very small numerical dissipation compared to other schemes, e.g., the Houbolt method [9, 16].

Time discretization approximates problem (1.5) by a sequence of quasistatic problems that can be written as an equivalent nonconvex constrained problem:

$$\boldsymbol{x}_{k+1} = \arg\min_{\boldsymbol{y} \in K} J(\boldsymbol{y}),\ J(\boldsymbol{y}) = \frac{1}{2} \int_0^L \left(\frac{\rho_s}{\Delta t^2} |\boldsymbol{y}|^2 + EI\alpha \left|\boldsymbol{y}''\right|^2 \right) ds - \int_0^L \boldsymbol{b} \cdot \boldsymbol{y}\, ds\,, \tag{1.27}$$

where $\boldsymbol{b}$ accounts for all the terms involving known quantities.

To treat the inextensibility condition $|\boldsymbol{y}'| = 1$, which is a quadratic constraint, we use an augmented Lagrangian method (e.g., [16, 33, 38, 41]). Let us introduce the

following space and sets:

$$\mathcal{V} = \left\{ \boldsymbol{y} \in (H^2(0,L))^2,\ \boldsymbol{y}(0) = \boldsymbol{a},\ \boldsymbol{y}'(0) = \boldsymbol{b} \right\},$$
$$\mathcal{V}_0 = \left\{ \boldsymbol{y} \in (H^2(0,L))^2,\ \boldsymbol{y}(0) = \boldsymbol{0},\ \boldsymbol{y}'(0) = \boldsymbol{0} \right\},$$
$$\mathcal{Q} = \left\{ \boldsymbol{q} \in (L^2(0,L))^2, |\boldsymbol{q}| = 1 \text{ a.e. on } (0,L) \right\}.$$

Problem (1.27) is equivalent to

$$\{\boldsymbol{x}_{k+1}, \boldsymbol{x}'_{k+1}\} = \arg\min_{\{\boldsymbol{y},\boldsymbol{q}\}\in W} J(\boldsymbol{y}), \quad \text{with} \quad W = \{\boldsymbol{y} \in V,\ \boldsymbol{q} \in \mathcal{Q},\ \boldsymbol{y}' - \boldsymbol{q} = \boldsymbol{0}\}.$$

With $r > 0$, we introduce the following augmented Lagrangian functional:

$$\mathcal{L}_r(\boldsymbol{y}, \boldsymbol{q}; \boldsymbol{\mu}) = J(\boldsymbol{y}) + \frac{r}{2}\int_0^L |\boldsymbol{y}' - \boldsymbol{q}|^2\, ds + \int_0^L \boldsymbol{\mu}\cdot(\boldsymbol{y}' - \boldsymbol{q})\, ds\,. \tag{1.28}$$

Let $\{\boldsymbol{x}, \boldsymbol{p}; \boldsymbol{\lambda}\}$ be a saddle point of $\mathcal{L}_r$ over $(\mathcal{V}\times\mathcal{Q})\times(L^2(0,L))^2$. Then a solution of problem (1.27) (and thus problem (1.26)) is $\boldsymbol{x}_{k+1} = \boldsymbol{x}$ and $\boldsymbol{p} = \boldsymbol{x}'_{k+1}$. In order to solve the above saddle-point problem, we employ the algorithm called ALG2 in, e.g., [33, 41]. As shown in, e.g., [33], this Uzawa-type algorithm is in fact a "disguised" Douglas–Rachford operator-splitting scheme:

– **Step 0**: The initial guess $\{\boldsymbol{x}_{-1}, \boldsymbol{\lambda}_0\} \in \mathcal{V}\times(L^2(0,L))^2$ is given.

Then, for $j \geq 0$, $\{\boldsymbol{x}_{j-1}, \boldsymbol{\lambda}_j, \}$ being known, proceed with:

– **Step 1**: Find $\boldsymbol{p}_j \in \mathcal{Q}$ such that:

$$\mathcal{L}_r(\boldsymbol{x}_{j-1}, \boldsymbol{p}_j; \boldsymbol{\lambda}_j) \leq \mathcal{L}_r(\boldsymbol{x}_{j-1}, \boldsymbol{q}; \boldsymbol{\lambda}_j), \quad \forall \boldsymbol{q} \in \mathcal{Q}.$$

– **Step 2**: Find $\boldsymbol{x}_j \in \mathcal{V}$ such that:

$$\mathcal{L}_r(\boldsymbol{x}_j, \boldsymbol{p}_j; \boldsymbol{\lambda}_j) \leq \mathcal{L}_r(\boldsymbol{y}, \boldsymbol{p}_j; \boldsymbol{\lambda}_j), \quad \forall \boldsymbol{y} \in \mathcal{V}_0\,. \tag{1.29}$$

– **Step 3**: Update the Lagrange multipliers by:

$$\boldsymbol{\lambda}_{j+1} = \boldsymbol{\lambda}_j + r((\boldsymbol{x}_j)' - \boldsymbol{p}_j).$$

To obtain $\boldsymbol{p}_j$ at step 1, we have to solve the minimization problem:

$$\min_{|\boldsymbol{q}|=1} \mathcal{L}_r(\boldsymbol{x}_{j-1}, \boldsymbol{q}; \boldsymbol{\lambda}_j), \text{ with the solution } \boldsymbol{p}_j = \frac{r(\boldsymbol{x}_{j-1})' + \boldsymbol{\lambda}_j}{|r(\boldsymbol{x}_{j-1})' + \boldsymbol{\lambda}_j|}\,. \tag{1.30}$$

Problem (1.29) can be stated as the equivalent problem: Find $\boldsymbol{x}_j \in \mathcal{V}$ such that for all $\boldsymbol{y} \in \mathcal{V}_0$:

$$\int_0^L \rho_s \frac{\boldsymbol{x}_j}{\Delta t^2}\cdot\boldsymbol{y}ds + \int_0^L EI\alpha\boldsymbol{x}_j''\cdot\boldsymbol{y}''ds + r\int_0^L \boldsymbol{x}_j'\cdot\boldsymbol{y}'ds$$
$$= \int_0^L \boldsymbol{b}\cdot\boldsymbol{y}ds + \int_0^L (r\boldsymbol{p}_j - \boldsymbol{\lambda}_j)\cdot\boldsymbol{y}'ds.$$

For the space discretization of problem (1.29) we use a third-order Hermite finite element method (e.g., [16]). For details about the discretization of $\boldsymbol{p}_j \in \Omega$ (1.30) and $\boldsymbol{\lambda}_j \in (L^2(0, L))^2$ we refer to [41].

Steps 1, 2, and 3 are repeated until the following stopping criterion

$$\left(\int_0^L \left| \frac{\partial}{\partial s} \boldsymbol{x}^i - \boldsymbol{p}^i \right|^2 ds \right)^{1/2} \leq \epsilon \tag{1.31}$$

is satisfied for a given tolerance $\epsilon > 0$, or the number of iterations exceeds a given number.

Once (1.31) is satisfied, we set $\tilde{\boldsymbol{x}}_{k+1} = \boldsymbol{x}^i$, which defines the new structure position before relaxation.

Remark 1.1. It is known that parameter r plays a fundamental role for the convergence of algorithm ALG2, as was pointed out in [26]. We adopt the same adaptive strategy presented in [26], i.e., we start with an initial guess $r = r_0$, where r_0 is a fixed number (for instance in the range of the flexural stiffness EI). Once the Augmented Lagrangian algorithm terminates, we check if termination criterion (1.31) is met. In case (1.31) is violated, the value of r is increased (e.g., by a factor of 10) and ALG2 is repeated with the new value of r.

1.5.3 Enforcement of the coupling conditions

To describe the enforcement of the coupling conditions reported in Section 1.2.3, we first recall that at every time step the fluid mesh is aligned with the structure position. However, in general the fluid and structure meshes do *not* coincide, since they are made up of different elements: cubic Hermite elements on the structure side, and quadratic isoparametric edges on the fluid side. Because of the alignment, the fluid nodes that approximate the interface are always located on the structure mesh, as shown in Figure 1.4. In Figure 1.4, we denote by $\Gamma_h^{f,n}$ the approximation of the location of Γ^n given by the fluid mesh, and by $\Gamma_h^{s,n}$ the approximation of Γ^n by the structure mesh.

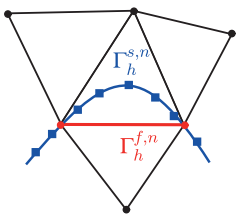

Fig. 1.4: Fluid triangulation (black) aligned with the structure mesh $\Gamma_h^{s,n}$ (blue). The fluid nodes are marked with dots, while the structure nodes are marked with squares. $\Gamma_h^{f,n}$ (red) is the approximation of the interface given by an edge of the fluid mesh.

Since Robin boundary condition (1.21) is a linear combination of the kinematic coupling condition and the dynamic coupling condition, we will only discuss the enforcement of the latter two conditions.

Enforcement of the kinematic coupling condition, i.e., the Dirichlet condition (1.18). Denote by $U_{\Gamma,k}$ and $\dot{X}_k$ the arrays of the nodal values of the corresponding fluid and structure velocities at the interface. Let B^n_{fs} be the interpolation matrix of the structure mesh at the fluid interface nodes. To impose Dirichlet condition (1.18), we set

$$U_{\Gamma,k+1} = B^n_{\text{fs}} \dot{X}_k \,. \tag{1.32}$$

Enforcement of the dynamic coupling condition. The fluid load onto the structure is given by the hydrodynamic force (1.9). The computation of the hydrodynamic force (1.9) is crucial for the numerical stability and accuracy of Domain Decomposition FSI solvers [30]. In the setting considered in this paper (an immersed beam), the quality of approximation of the pressure jump across the beam is of great importance, as demonstrated by the results in Section 1.6.2.

The load exerted by the fluid onto the structure $\boldsymbol{f}_\Gamma$ can be computed as the variational residual $\mathcal{R}$ of the momentum conservation equation for the fluid, tested with test functions $\boldsymbol{v}$ that are different from zero on $\Gamma(t)$:

$$\begin{aligned}\int_{\Gamma(t)} \boldsymbol{f}_\Gamma \cdot \boldsymbol{v} \, \mathrm{d}\Gamma = &-\rho_{\text{f}} m\Big(\Omega_{\text{f}}(t); \frac{\partial \boldsymbol{u}}{\partial t}\Big|_{\hat{\mathbf{x}}}, \boldsymbol{v}\Big) - \rho_{\text{f}} c(\Omega_{\text{f}}(t); \boldsymbol{u} - \mathbf{w}; \boldsymbol{u}, \boldsymbol{v}) \\ &- a(\Omega_{\text{f}}(t); \boldsymbol{u}, \boldsymbol{v}) - b(\Omega_{\text{f}}(t); p, \boldsymbol{v}) \\ &= \mathcal{R}(\Omega_{\text{f}}(t); \boldsymbol{u}, p, \boldsymbol{v}) \,. \end{aligned} \tag{1.33}$$

Let $\boldsymbol{f}^f_{\Gamma,k+1}$ denote the discrete hydrodynamic force at $\Gamma^{f,n}_h$ and subiteration $k+1$. After time and space discretization of (1.33), $\boldsymbol{f}^f_{\Gamma,k+1}$ is calculated from:

$$\int_{\Gamma^{f,n}_h} \boldsymbol{f}^f_{\Gamma,k+1} \cdot \boldsymbol{v}_h \, \mathrm{d}\Gamma = \mathcal{R}(\Omega^n_{\text{f}}; \boldsymbol{u}_{h,k+1}, p_{h,k+1}, \boldsymbol{v}_h) \,. \tag{1.34}$$

By using matrix notation, Equation (1.34) can be written as follows:

$$M^{n,f}_\Gamma F^f_{\Gamma,k+1} = R_{k+1}, \ , \tag{1.35}$$

where $F^f_{\Gamma,k+1}$ is the array of nodal values of $\boldsymbol{f}^f_{\Gamma,k+1}$, $M^{n,f}_\Gamma$ is the mass matrix at $\Gamma^{f,n}_h$, and R_{k+1} corresponds to the known values of the combined residuals appearing on the right-hand side of Equation (1.34). This defines the hydrodynamic force, calculated at the fluid mesh nodes along the beam.

To enforce the dynamic coupling condition (1.11), this hydrodynamic force needs to be set equal to the structural load $\boldsymbol{f}$ exerted onto the fluid. For this purpose, we need to assign the values of the hydrodynamic force to the structure mesh nodes $\Gamma^{s,n}_h$ which

do not necessarily lie on the structure discretization defined by the fluid mesh, see Figure 1.4. To do that, we first project the structure mesh nodes of $\Gamma_h^{s,n}$ onto the fluid mesh interface $\Gamma_h^{f,n}$. At the fluid mesh, the fluid loading onto the structure $\boldsymbol{f}_{\Gamma,k+1}^f$ is defined by the process described above. We take those values of $\boldsymbol{f}_{\Gamma,k+1}^f$ and interpolate them first along the edges of the fluid mesh at the *projected* structural nodes, and then we assign those values back to the *original* structure nodes. More precisely, whenever the structural load $\boldsymbol{f}_{k+1}(\mathbf{x})$ needs to be evaluated for some $\mathbf{x} \in \Gamma_h^{s,n}$ (for instance at the quadrature nodes needed to evaluate the right-hand side of Equation (1.26)), we first define the projected structure node

$$\tilde{\mathbf{x}} := \operatorname*{arg\,min}_{\mathbf{y} \in \Gamma_h^{f,n}} \|\mathbf{x} - \mathbf{y}\|$$

and then let $\boldsymbol{f}_{k+1}(\mathbf{x}) = \boldsymbol{f}_{\Gamma,k+1}^f(\tilde{\mathbf{x}})$. We use the following notation to summarize this procedure:

$$F_{\Gamma,k+1}^s = B_{\mathrm{sf}}^n F_{\Gamma,k+1}^f \,, \tag{1.36}$$

where we used B_{sf}^n to denote the extrapolation of the values of the hydrodynamic quantities at the fluid nodes onto the structure nodes. This defines the hydrodynamic force at the *structure mesh nodes*, and enforces the dynamic coupling condition (1.11).

It is important to notice that in this numerical implementation of the dynamic coupling condition, the power exchanged between the fluid and structure is not perfectly balanced, i.e., at the discrete level, the energy imparted by the fluid onto the structure is not perfectly converted into the total energy of the structure, and vice versa. This is due to the nonmatching fluid and structure meshes. In the case of the DN algorithm, this mismatch can be precisely quantified as follows.

At the time t^{n+1}, after the convergence of the DN subiterations, the discrete power exchanged at the interface from the fluid side is

$$\begin{aligned} P^{f,n+1} &= \int_{\Gamma_h^{f,n+1}} \boldsymbol{f}_\Gamma^{f,n+1} \cdot \boldsymbol{u}_h^{n+1} \,\mathrm{d}\Gamma = (U_\Gamma^{n+1})^T M_\Gamma^{f,n+1} F_\Gamma^{f,n+1} \\ &= (\dot{X}^{n+1})^T (B_{\mathrm{fs}}^{n+1})^T M_\Gamma^{f,n+1} F_\Gamma^{f,n+1} \,, \end{aligned} \tag{1.37}$$

where for the last equation we used (1.32). Similarly, the discrete power exchanged at the interface from the structure side is

$$\begin{aligned} P^{s,n+1} &= \int_{\Gamma_h^{s,n+1}} \boldsymbol{f}_\Gamma^{s,n+1} \cdot \dot{\boldsymbol{x}}_h^{n+1} \,\mathrm{d}\Gamma = (\dot{X}^{n+1})^T M_\Gamma^{s,n+1} F_\Gamma^{s,n+1} \\ &= (\dot{X}^{n+1})^T M_\Gamma^{s,n+1} B_{\mathrm{sf}}^{n+1} F_\Gamma^{f,n+1} \,, \end{aligned} \tag{1.38}$$

where for the last equation we used (1.36). Thus, the power exchanged at the interface is balanced if

$$(B_{\mathrm{fs}}^{n+1})^T M_\Gamma^{f,n+1} = M_\Gamma^{s,n+1} B_{\mathrm{sf}}^{n+1} .$$

Since $\Gamma_h^{f,n+1}$ and $\Gamma_h^{s,n+1}$ are aligned but do not coincide ($\Gamma_h^{s,n+1}$ is a piecewise cubic globally C^1 function, and $\Gamma_h^{f,n+1}$ is a piecewise quadratic interpolation) and the fluid and structure discretizations are based on different elements, the balance equation is not necessarily fulfilled exactly. However, in Section 1.6.3 we will show that the difference between $P^{f,n+1}$ and $P^{s,n+1}$ is very small (0.01% of the power value) in our computations.

1.6 Numerical results

A series of numerical tests is presented that showcase the main features and performance of our approach. In all the tests, the fluid density of $\rho_f = 1\ \mathrm{g/cm^3}$ is considered, the structure mesh always consists of 45 nodes (with cubic Hermite elements), and the stopping tolerance in (1.19) for the partitioned schemes (either DN or RN) is always set to $\epsilon_{FS} = 10^{-8}$. We use the SI unit system, and present all the quantities in the centimeter-gram-second (CGS) units. If the units of a certain quantity are omitted for the sake of simplicity, it is implied that they are in the CGS system.

1.6.1 Validation of the structure solver

The purpose of this section is to validate the structure solver by a benchmark with an exact solution.

We consider $s \in [0, \pi/2]$ and $t \in [0, 1]$, and a family of exact solutions which is given by:

$$\boldsymbol{x}_{ex}(s,t) = (\phi(t))^{-1} \left[\cos(s\phi(t)), \sin(s\phi(t))\right]^T . \tag{1.39}$$

Notice that solution (1.39) satisfies the inextensibility condition $|\boldsymbol{x}|' = 1$ pointwise for every function $\phi(t)$. We chose $\phi(t) = e^t$, for which the solution is a quarter of a circle of initial radius 1 that coils over time as its radius decreases (Figure 1.5). At $s = 0$ and $s = \pi/2$, we impose the values of $\boldsymbol{x}$ and $\boldsymbol{x}'$. The forcing term $\boldsymbol{f}_{ex}$ needed to recover solution (1.39) is found by plugging $\boldsymbol{x}_{ex}$ into the governing differential equations (strong form):

$$\rho_s \ddot{\boldsymbol{x}}_{ex} + EI\boldsymbol{x}_{ex}'''' = \boldsymbol{f}_{ex} . \tag{1.40}$$

For simplicity, we set $\rho_s = 1\ \mathrm{Kg/m^3}$ and $EI = 1\ \mathrm{Kg\,m^3/s^2}$. The forcing term $\boldsymbol{f}_{ex}$ is made up of two contributions: an external body force $\boldsymbol{f}_b$ and an internal force due to inextensibility $\boldsymbol{f}_{in}$. To find $\boldsymbol{f}_{in}$, we notice that problem (1.5) is equivalent to minimization problem $\boldsymbol{x} = \arg\min_{\boldsymbol{y}\in K} J(\boldsymbol{y})$, where the total energy of the beam can be written as:

$$J(\boldsymbol{y}) = \frac{1}{2}\int_0^L \rho_s|\ddot{\boldsymbol{y}}|^2 ds + \frac{1}{2}\int_0^L EI\left|\boldsymbol{y}''\right|^2 ds + \frac{1}{2}\int_0^L \lambda(|\boldsymbol{y}'|^2 - 1)ds - \int_0^L \boldsymbol{f}\cdot\boldsymbol{y} ds,$$

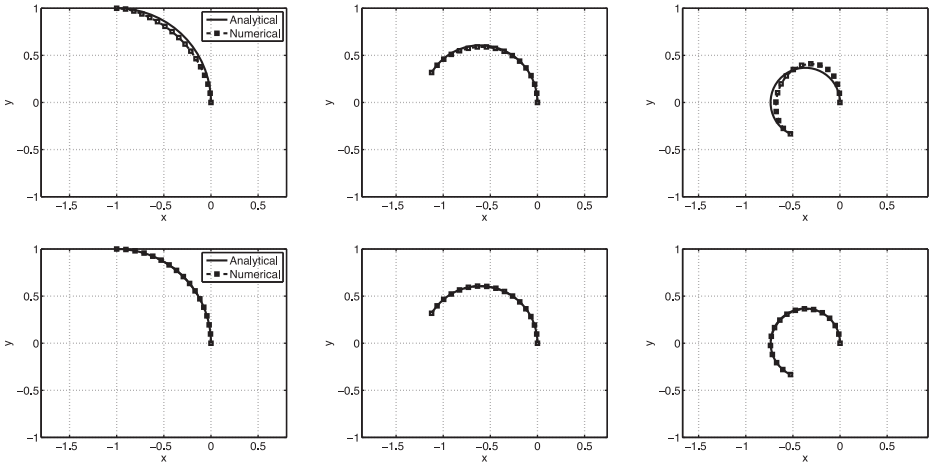

Fig. 1.5: Comparison between analytical and numerical solution at $t = 0$ s (left), $t = 0.5$ s (center), $t = 1$ s (right) for two values of stopping tolerance: $\epsilon = 10^{-1}$ (top) and $\epsilon = 10^{-5}$ (bottom). The legend in the subfigures on the left is common to all the subfigures.

and λ is a scalar function that depends on time only. If the above functional attains its minimum at $\boldsymbol{x}$, it follows that its Gâteaux derivative must be vanishing at $\boldsymbol{x}$, leading to

$$\int_0^L \rho_s \ddot{\boldsymbol{x}} \cdot \boldsymbol{y} ds + \int_0^L EI\, \boldsymbol{x}'' \cdot \boldsymbol{y}'' ds = \int_0^L \boldsymbol{f} \cdot \boldsymbol{y} ds + \int_0^L (\lambda \boldsymbol{x}')' \cdot \boldsymbol{y} ds,$$

for all $\boldsymbol{y} \in dK(\boldsymbol{x})$. The second integral on the right-hand side (equal to zero if $\boldsymbol{y} \in dK(\boldsymbol{x})$, which is not the case for the test functions used in the computations) gives the explicit contribution of $\boldsymbol{f}_{\text{in}}$.

We are going to check the convergence rates in time for the generalized Crank–Nicolson scheme in Section 1.5.2 with $\alpha = 1/4$ in two cases:

- linear case: when the forcing term is $\boldsymbol{f}_{\text{ex}}$ the inextensibility condition becomes inactive due to the fact that $\boldsymbol{f}_{\text{ex}}$ is given by (1.40) and the problem reduces to the linear beam equation;
- nonlinear case: when then forcing term is $\boldsymbol{f}_{\text{ex}} + (\lambda \boldsymbol{x}')'$, with, e.g., $\lambda = 1$, the problem becomes nonlinear and the inextensibility is treated via the augmented Lagrangian method described in Section 1.5.2.

The space resolution Δs is taken to be $\pi/240$. In the nonlinear case, for ALG2 we set stopping tolerance $\epsilon = 10^{-5}$ (1.31) and $r = 10^2$. In Figure 1.6, we plot the L^2 norm of the difference between the exact solution $\boldsymbol{x}_{\text{ex}}$ and the numerical solution $\boldsymbol{x}_h$ at $t = 1$ against time step ($\Delta t = 0.2, 0.1, 0.05, 0.025, 0.0125, 0.00625$) for the linear and non-

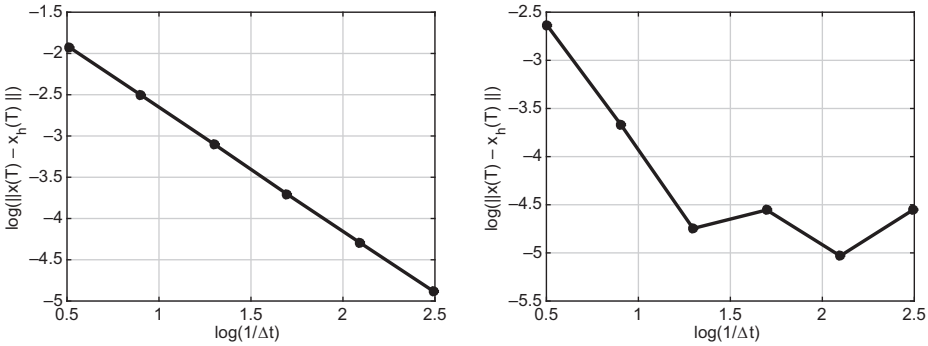

Fig. 1.6: Convergence rate in time for the generalized Crank–Nicolson scheme in the linear (left) and nonlinear/inextensible (right) case.

linear cases. The rate predicted by the theory (second order) is achieved in the linear case. In the nonlinear case, the order of convergence is even larger than 2 provided that Δt is less than a critical value for which the error reaches the stopping tolerance ϵ. If Δt is greater than that critical value, the error remains unchanged or even slightly increases.

To illustrate that the error depends on the choice of ϵ, in Figure 1.5, we compare analytical solution (1.39) with the numerical solution at $t = 0, 0.5, 1\,\mathrm{s}$ and for two values of the stopping tolerance: $\epsilon = 10^{-1}$ (top) and $\epsilon = 10^{-5}$ (bottom), every other discretization parameter being the same. For $\epsilon = 10^{-1}$ the difference between analytical and numerical solution is clearly visible, while for $\epsilon = 10^{-5}$ the two solutions are almost superimposed.

Finally, in order to evaluate the dependence of the error on ϵ, we report in Figure 1.7 the convergence rates in time in the nonlinear case for different values of the stopping tolerance $\epsilon = 10^{-2}, 10^{-3}, 10^{-4}, 10^{-5}, 10^{-6}, 10^{-7}$. The values for Δt and Δs are the same as those used for the results in Figure 1.6. We see that at the critical value of Δt the curves reach a plateau for all the values of ϵ, indicating that for a given value of ϵ it does not make sense to choose a time-step size that is too small. Our computations seem to indicate that Δt should be larger than $\sqrt{\epsilon}$.

In the following sections, for the Augmented Lagrangian method in Section 1.5.2, we take $\epsilon = 10^{-4}$ in (1.31), and at the beginning of the simulation we set $r_0 = 10^{-4}$; see Remark 1.1.